Oscillatory waveform shape and temporal spike correlations differ across bat frontal and auditory cortex

Abbreviated title: Oscillatory waveform shape in the bat cortex

Authors: Francisco García-Rosales[1*], Natalie Schaworonkow[1], Julio C. Hechavarria[2].
Affiliations: [1] Ernst Strüngmann Institute (ESI) for Neuroscience in Cooperation with Max Planck Society, 60528 Frankfurt am Main, Germany; [2] Institut für Zellbiologie und Neurowissenschaft, Goethe-Universität, 60438 Frankfurt/M., Germany.
[*] *Corresponding author.*

Mailing address: Francisco García-Rosales, Ernst Strüngmann Institute (ESI) for Neuroscience in Cooperation with Max Planck Society, Deutschordenstraße 46, 60528 Frankfurt am Main, Germany; Tel. (+49) 69 / 96769 123. Email: francisco.garcia-rosales@esi-frankfurt.de

Number of pages: 26

Number of figures: 7

Number of words (Abstract): 207

Number of words (Introduction): 650

Number of words (Discussion): 1421

Conflict of interests: The authors declare no conflicting financial or non-financial interests.

Acknowledgments: This work was supported by the DFG (Grant No. HE 7478/1-1, to J.C.H.), the Joachim-Herz Foundation (fellowship granted to F.G.R.), and a Marie Skłodowska-Curie Actions Postdoctoral Fellowship (grant No. 101062497, to N.S.).

Abstract

Neural oscillations are associated with diverse computations in the mammalian brain. The waveform shape of oscillatory activity measured in cortex relates to local physiology, and can be informative about aberrant or dynamically changing states. However, how waveform shape differs across distant yet functionally and anatomically related cortical regions is largely unknown. In this study, we capitalize on simultaneous recordings of local field potentials (LFPs) in the auditory and frontal cortices of awake *Carollia perspicillata* bats to examine, on a cycle-by-cycle basis, waveform shape differences across cortical regions. We find that waveform shape differs markedly in the fronto-auditory circuit even for rhythmic activity in comparable frequency ranges (i.e. in the delta and gamma bands) during spontaneous activity. In addition, we report consistent differences between areas in the variability of waveform shape across individual cycles. A conceptual model predicts higher spike-spike and spike-LFP correlations in regions with more asymmetric shape, a phenomenon that was observed in the data: spike-spike and spike-LFP correlations were higher in frontal cortex. The model suggests a relationship between waveform shape differences and differences in spike correlations across cortical areas. Altogether, these results indicate that oscillatory activity in frontal and auditory possess distinct dynamics related to the anatomical and functional diversity of the fronto-auditory circuit.

Significance statement

The brain activity of many animals displays intricate oscillations, which are usually characterized in terms of their frequency and amplitude. Here, we study oscillations from the bat frontal and auditory cortices on a cycle-by-cycle basis, additionally focusing on their characteristic waveform shape. The study reveals clear differences across regions in waveform shape and oscillatory regularity, even when the frequency of the oscillations is similar. A conceptual model predicts that more asymmetric waveforms result from stronger correlations between neural spikes and electrical field activity. Such predictions were supported by the data. The findings shed light onto the unique properties of different cortical areas, providing key insights into the distinctive physiology and functional diversity within the fronto-auditory circuit.

Introduction

Rhythmic neural activity at various timescales underpins several functions in the mammalian brain. In the frontal cortex, oscillations of local-field potentials (LFPs) in low and high frequencies are implicated in cognitive and executive control (Helfrich and Knight, 2019; Insel et al., 2012; Rajan et al., 2019; Tavares and Tort, 2022; Veniero et al., 2021; Zhang et al., 2016), while rhythmic activity in sensory cortices is linked with the effective encoding of incoming stimuli (Gourevitch et al., 2020; Gross et al., 2007; Kienitz et al., 2021; Lakatos et al., 2007; Tan et al., 2019; Teng et al., 2017; Uran et al., 2022). These oscillations reflect the underlying dynamics of their generating motifs, which determine several of their properties, including waveform shape (Cole and Voytek, 2017). Indeed, waveform shape and related features change in the developing brain (Schaworonkow and Voytek, 2021) and possess atypical characteristics in disease (Cole and Voytek, 2019; Cole et al., 2017; Jackson et al., 2019). Waveform patterns of oscillatory activity can provide important insights into the physiology and function of the neocortex, yet how they differ across cortical regions remains largely unstudied.

In this work, we examine oscillatory waveform shape in the frontal and auditory cortices of a mammalian vocal specialist, the bat *Carollia perspicillata*. The bat auditory cortex (AC) is a well-studied structure that presents both spontaneous and stimulus-driven rhythmic patterns of neuronal activity (Garcia-Rosales et al., 2019; Hechavarria et al., 2016; Medvedev and Kanwal, 2004). As in other mammals (Lakatos et al., 2005; Luo and Poeppel, 2007; Neymotin et al., 2022; Teng et al., 2017), LFPs in the bat AC track the temporal dynamics of acoustic sequences with periodic and quasi-periodic temporal structures (Garcia-Rosales et al., 2018). LFPs in *C. perspicillata*'s AC exhibit clear coupling with neuronal spiking, potentially coordinating single-cell responses to acoustic stimuli and contributing actively to the encoding of multi-syllabic communication sounds (Garcia-Rosales et al., 2018).

In the frontal cortex, we focused on the frontal auditory field (FAF), a structure specialized in auditory-related behaviour (Eiermann and Esser, 2000; Kanwal et al., 2000; Kobler et al., 1987). This region is anatomically connected with the AC, but receives also relatively fast inputs from an alternative pathway bypassing midbrain and cortex (Kobler et al., 1987). Pre- and post-vocal dynamics in the FAF, as well as its functional connectivity patterns with the AC and the striatum, implicate this region in the control of vocalization behaviour (Garcia-Rosales et al., 2022; Weineck et al., 2020). Furthermore, the FAF is anatomically connected with the superior colliculus, suggesting that it may be involved in coordinating fast movements based on the bat's auditory environment (Casseday et al., 1989; Kobler et al., 1987). The nature of FAF-AC interconnectivity suggests that the FAF plays a crucial role in the integration of auditory feedback for the coordination of rapid auditory-based behaviour (Garcia-Rosales et al., 2022). These data indicate that, while the AC operates as a classical sensory cortex, the FAF acts as part of a control and integration hub.

While low- and high-frequency oscillatory activities in the bat FAF-AC network are functionally related, it is unknown how they differ in terms of waveform shape. Characterizing waveform shape differences across cortical regions could be an informative step towards understanding how neuronal oscillations in these areas differ, and thus constrain hypotheses about the mechanisms underlying neural activity across structures. By means of simultaneous electrophysiological recordings and cycle-by-cycle analyses of neural oscillations, we show that the waveform shape and variability of frontal- and auditory-cortical oscillations differ markedly in delta and gamma frequencies. We demonstrate a relationship between waveform shape and spike correlations by modelling and computing spike-field measures. We argue that these differences reflect physiological disparities in the FAF-AC circuit, and establish a potential link between spike timing and waveform shape. Our results support the notion of heterogeneity of cortical rhythms in the mammalian brain, and stress the importance of waveform shape for understanding cortical physiology and function.

Results

Spectral properties of frontal and auditory cortical LFPs

A total of 29 paired penetrations in FAF and AC were performed in two bats, resulting in an equal number of simultaneous, multi-layer LFP recordings from both regions. Example frontal and auditory cortical LFP traces from one representative animal are given in **Fig. 1a** (note that data from the second animal was highly consistent). Direct visual inspection of the LFP signals revealed clear rhythmicity in low and high frequencies in both frontal and auditory cortices. Evidence for rhythmic activity was also clear in grand-average spectra obtained from ~20-min long LFPs in FAF and AC (**Fig. 1b, f**). “Bumps” in the spectrum can be understood as deviations from a 1/f power-law, a characteristic of aperiodic mesoscopic signals such as LFPs (Baranauskas et al., 2012), and therefore suggest the presence of brain oscillations. We confirmed that the spectral bumps were in fact deviations from the power-law by performing spectral parametrization and fitting of 1/f curves to the power spectral density from each individual recording (see Methods and (Donoghue et al., 2020)). Representative, parametrized spectra are depicted in **Fig 1c, g**, corresponding to the entire LFP trace of ~20 minutes from which the data in **Fig 1a** were selected. The 1/f fit is shown in dashed blue lines. Deviations in the spectra from the power-law trend were clear, particularly in the FAF. We tested whether such deviations were consistently present in all recordings by normalizing the power spectrum of each LFP trace (N = 15 in Bat-01, N=14 in Bat-02) to their fitted 1/f function (**Fig. 1d, h**). Power spectral values would hover around 0 in the absence of consistent deviations, but would be significantly above zero otherwise. Normalized spectral values were significantly above 0 in FAF and AC (FDR-corrected one-sample t-tests; $p_{corr} < 1.72x10^{-4}$, $t > 2.41$) at relatively low (~1-5 Hz in FAF and AC), intermediate (~12-27 Hz in AC), and relatively high (ranging from ~32-105 Hz, but peaking at 70-85 Hz in FAF and AC) frequencies (**Fig. 1e,i**).

In bats such as *C. perspicillata* (the animal studied here), LFP activity in low and high frequencies is related to vocal production (e.g. at frequencies delta: 1-4 Hz, beta: 12-30 Hz, and gamma: 60-120 Hz; see Garcia-Rosales et al. (2022); Weineck et al. (2020)). Considering the above and the patterns of deviations from a pure 1/f signal shown in **Fig. 1**, in subsequent analyses we focused on frequency bands delta (1-4 Hz) and gamma (65-85 Hz). Beta-band frequencies were not included because no clear peaks in this range were detected in FAF signals (**Fig. 1e,i**).

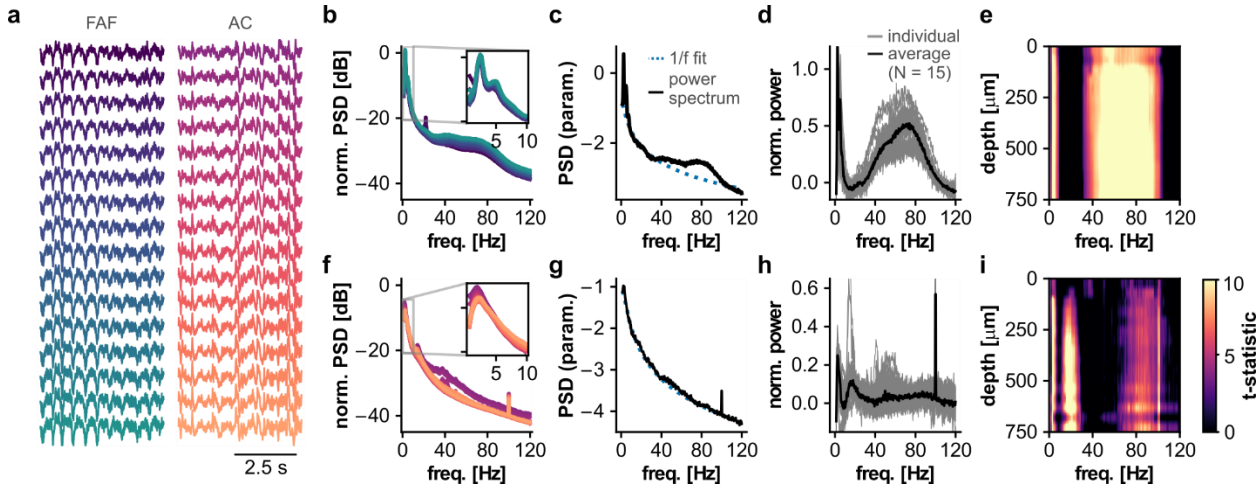

Figure 1. Spectral properties of local-field potentials in FAF and AC. (**a**) Cortical LFPs (5 s traces) recorded simultaneously from the FAF (left) and the AC (right; note that channel depths are colour-coded) of ***Bat-01***. (**b**) Average power spectra in FAF across all recordings (n = 15) in **Bat-01** using full LFP traces (lengths of ~20 minutes), for all channels. The spectrum of each channel is colour-coded according to the depth scheme of panel **a**. (**c**) Parametrization of an exemplary power spectrum obtained from ~20 minutes LFP recordings in the FAF (depth, 700 μm). LFP traces originate from the same penetration shown in **a**. The 1/f fit is depicted as a blue dashed line; power spectrum shown in solid black. (**d**) Normalized power spectra (to 1/f activity) across all recordings in **Bat-01**, shown for channels located at 700 μm in FAF. Solid black line indicates average (N = 15). (**e**) We tested whether the normalized power spectrum was significantly larger than 0 (FDR-corrected t-test, $p_{corr} < 0.05$) across depths and frequencies. The t-statistics are summarized here; values were set to 0 if the normalized power spectrum was not significantly (i.e. $p_{corr} >= 0.05$). (**f-i**) Similar to panels **b-e**, but data shown corresponds to channels located in the AC.

Differences in waveform shape between frontal and auditory cortical LFPs

To study the characteristics of delta- and gamma-band rhythmic activity in frontal and auditory areas, we performed a cycle-by-cycle analysis of the recorded LFP. Cycles were considered only if they were part of consistent oscillatory activity (i.e. they were associated with a putative oscillatory bursts). Bursts of oscillatory activity were detected using the *bycycle* algorithm (Cole and Voytek, 2019), which capitalizes on a time-domain approach for quantifying waveform shape (**Fig. 2a**). A burst is detected based on four parameters, which control for signal-to-noise ratio (SNR) and waveform consistency (see Methods). In this context, an oscillatory burst occurs if these threshold values of these parameters are exceeded for at least 3 consecutive cycles.

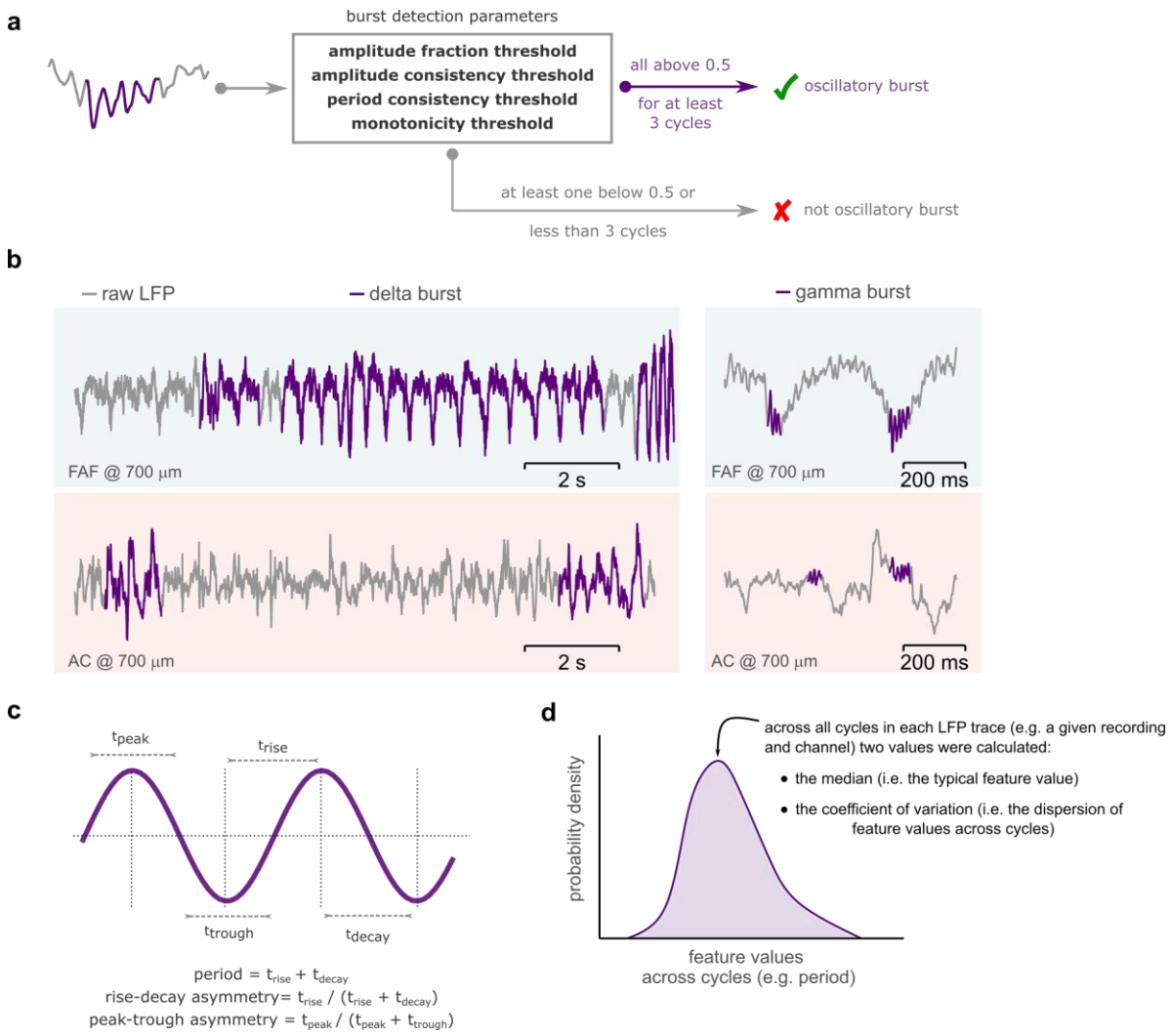

Figure 2. Burst cycle features and the coefficient of variation. (**a**) Schematic representation of the oscillatory burst detection algorithm. If at least 3 consecutive cycles fulfilled the detection parameters (enclosed in the box), these cycles together were considered as an oscillatory burst (marked in purple); otherwise, no burst was detected. No-burst cycles were not used in further analyses. (**b**) Representative delta- and gamma-frequency bursting activity (bursts marked in purple) in the FAF and AC, at a cortical depth of 700 μm. (**c**) Illustration of cycle waveform features: period, rise-decay asymmetry, and peak-trough asymmetry. An artificial sinusoidal waveform was utilized for illustrative purposes. (**d**) The median value for a given feature (e.g. period) across all cycles was used as the value of that feature for a given LFP trace. The coefficient of variation across all feature values was used as a measure of dispersion.

Representative burst events in delta- and gamma-bands are shown for FAF and AC in **Fig. 2b**. Bursts were typically more frequent in the frontal cortex, being also notably different in shape to their auditory cortical counterparts. Differences in the waveform shape of oscillatory activity were quantified by measuring three main features on a cycle-by-cycle basis: cycle period, cycle rise-decay asymmetry, and cycle peak-trough asymmetry (**Fig. 2c**; Cole and Voytek (2019)). Specifically, we performed systematic channel-by-channel pairwise comparisons to determine the consistency of waveform differences across recording locations. For each LFP trace, the median feature value across all detected cycles was considered the waveform shape feature for that trace. Thus, for a given electrode, 29 values (one value per recording) of waveform shape features were considered. This allowed us to conduct paired statistical testing, capitalizing on the fact that electrophysiological measurements were conducted simultaneously in

the AC and the FAF. Note that the median summarizes a distribution of feature values, yielding one value per channel and recording. In this study, median values were quantified, for each LFP trace, from hundreds of cycles (minimum number of cycles across all recordings and channels in the delta band: 623.44 +- 9.15 in FAF, and 492.44 +- 15.13 in AC; in the gamma band: 759.88 +- 21.16 in FAF, and 303.88 +- 19.42 in AC; mean +- s.e.m).

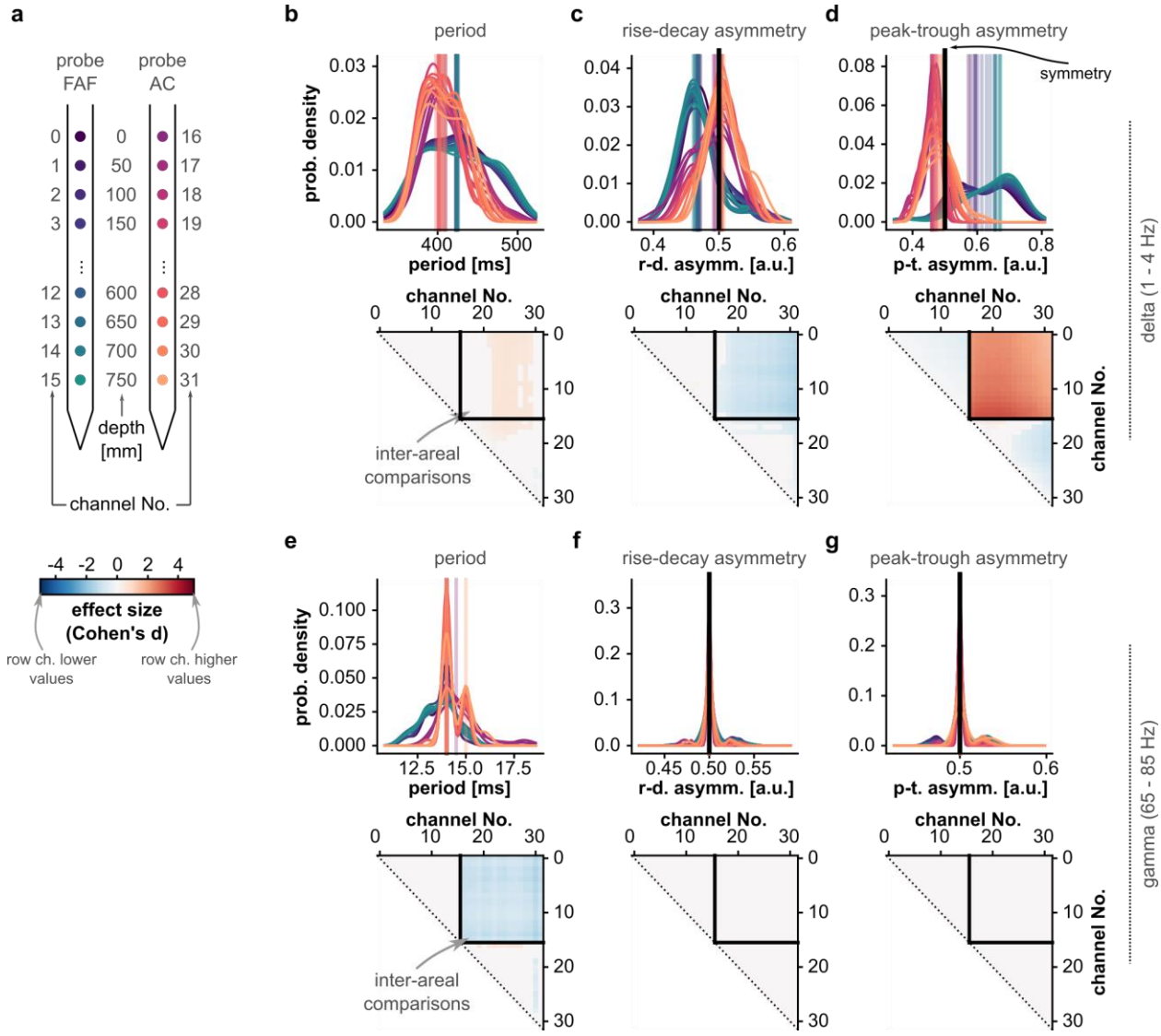

Figure 3. Waveform shape differences between frontal and auditory cortical LFPs. (**a**) Schematic illustrating the relationship of region and cortical depth with the channel number markers of panels **b**-**g**. Notice that depths are colour-coded as in **Fig. 1** in the main text. (**b**) *Top*: Distribution of oscillatory cycle periods across all penetrations (N = 29; for each penetration, the median period across all cycles is considered), for all channels (in FAF and AC; see panel **a** for region and depth according to colour), in the delta band. Vertical lines indicate the median of each distribution. *Bottom*: Effect sizes of pairwise statistical comparisons of population-level period values across all channels (FDR-corrected Wilcoxon signed-rank tests). Effect sizes for comparisons that did not yield significance (i.e. p_{corr} >= 0.05) were set to 0. A cell (*r, c*) in the effect size matrix indicates the effect size of the comparison between CV values in channel *r* and channel *c* (as per panel **a**). The quadrant spanning rows [0-15] and columns [16-31] illustrates effect sizes of comparisons between channels in FAF and AC. In this quadrant, blue colours indicate lower periods in FAF. (**c**) Same as in **b**, but corresponding to values of cycle feature "rise-decay asymmetry". (**d**) Same as in **c**, but related to values of cycle feature "peak-trough asymmetry". (**e**-**g**) Same as **b**-**d**, but shown for values obtained using gamma-band oscillatory cycles.

The distribution of feature values across recordings is given in **Fig. 3b-d** (top) for delta frequencies, and in **3e-g** (top) for gamma frequencies, across all channels (see **Fig. 3a**). Channel-by-channel comparisons revealed significant differences across cortical regions (FDR-corrected Wilcoxon signed-rank tests, significance when $p_{corr} < 0.05$). These analyses are summarized in the comparison matrices of **Fig. 3b-g** (bottom). A comparison matrix represents the effect sizes (d) of pairwise comparisons of feature values across channels (|d| < 0.5 small, 0.5 <= |d| <= 0.8 medium, |d| > 0.8 large effect sizes; Cohen (2013)). A cell (*r, c*) in the matrix illustrates the effect size of comparing median values from a channel indexed by row *r*, and a channel indexed by column *c* (i.e. channel *r* vs. channel *c*). The relationship between a channel index and its relative depth in frontal or auditory cortex is schematized in **Fig. 3a**. The upper right quadrant of each matrix represents comparisons of channels in FAF vs. those in AC. Only effect size values of significant comparisons ($p_{corr} < 0.05$) were shown; they were set to 0 otherwise.

Delta-band oscillatory cycles in frontal and auditory cortices differed in period with typically medium effect sizes (0.5 < |d| <= 0.8; **Fig. 3b**,**e**), but were strongly different in terms of their temporal asymmetries (Fig. **3c-d**, bottom; |d| > 0.8). This is readily visible in the examples of **Fig. 2b**, where the troughs in FAF delta oscillations were notably sharper than the peaks, a less evident phenomenon in the AC. The data in **Fig. 3** show that such patterns were consistent across recordings. The period of gamma-band cycles in FAF and AC differed more markedly than that of delta-band cycles (**Fig. 3e,** bottom; |d| > 0.8), yet gamma-band cycles did not differ in their asymmetry across structures, with values also suggesting that gamma cycles were relatively temporally symmetric (i.e. asymmetry values close to 0.5) in both areas.

By examining recordings independently, we observed that beyond direct differences in waveform shape features (or lack thereof), feature values in FAF were typically less variable than those measured in the AC. We thus quantified and compared the dispersion of waveform shape features as the coefficient of variation (CV; **Fig. 2d**) for each LFP trace. A larger CV indicates that cycle features vary over a wider range of parameters, suggesting higher variability in the oscillatory processes. Like the median, the CV summarizes a distribution, yielding one value per LFP trace (see above). The same cycles used to calculate median feature values were used to calculate CV values.

The distributions of CV values across cycle features for each channel are given in **Fig. 4b-d** (top) for delta frequencies, and **Fig. 4e-g** (top) for gamma frequencies. CV values appeared consistently lower for channels in FAF than for those in AC. This trend was confirmed by statistical, channel-by-channel pairwise comparisons (FDR-correct Wilcoxon signed-rank tests, significance when $p_{corr} < 0.05$), summarized in comparison matrices similar to those of **Fig. 3**. Statistical comparisons between channels located in different regions (the upper right quadrants of the comparison matrices) yielded the highest effect sizes (typically |d| > 0.8, large). CV values were consistently and significantly lower in FAF channels than in AC channels, in delta- and gamma frequency bands, for all cycle features. Some significant within-area differences also occurred (e.g. deeper channels in FAF had higher CV values than more

superficial ones), yet effect sizes were typically medium (0.5 < |d| < 0.8) or small (|d| < 0.5). Overall, these results indicate that, beyond first-order differences in waveform shape, oscillatory activity in the frontal cortex exhibits a higher degree of cycle-by-cycle regularity (i.e. lower variability over cycles) than that of the AC.

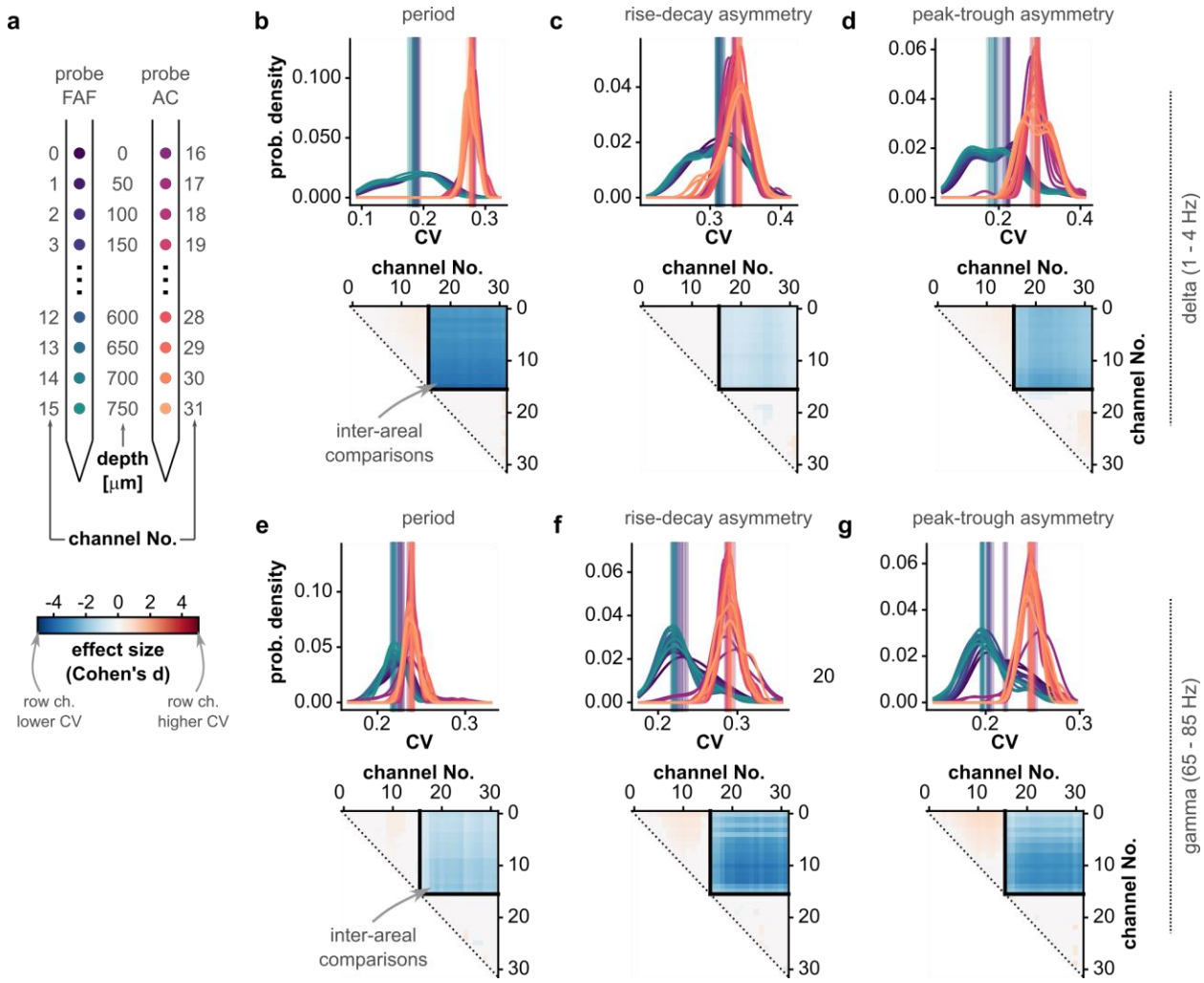

Figure 4. The dispersion of waveform shape parameter differs between frontal and auditory regions. (**a**) Schematic illustrating the relationship of region and cortical depth with the channel number markers of panels **b**-**g**. Notice that depths are colour-coded as in **Fig.1**. (**b**) *Top*: Distribution of CV values for oscillatory cycle periods across all penetrations (N = 29), for all channels (in FAF and AC; see panel **a** for region and depth according to colour), in the delta band. Vertical lines indicate the median of each distribution. *Bottom*: Effect sizes of pairwise statistical comparisons of population CV values across all channels (FDR-corrected Wilcoxon signed-rank tests). Effect sizes for comparisons that did not yield significance (i.e. p_{corr} >= 0.05) were set to 0. A cell (*r, c*) in the effect size matrix indicates the effect size of the comparison between CV values in channel *r* and channel *c* (as per panel **a**). The quadrant spanning rows [0-15] and columns [16-31] illustrates effect sizes of comparisons between channels in FAF and AC. In this quadrant, blue colours indicate lower CV values in FAF. (**c**) Same as in **b**, but corresponding to CV values of cycle feature "rise-decay asymmetry". (**d**) Same as in **c**, but related to CV values of cycle feature "peak-trough asymmetry". (**e**-**g**) Same as **b**-**d**, but shown for CV values obtained using gamma-band oscillatory cycles. (Effect sizes can be interpreted as follows: |d| < 0.5 small, 0.5 <= |d| <= 0.8 medium, |d| > 0.8 large).

Differences across regions are robust against burst detection parameters

The data indicate that oscillations in the FAF are more regular than those in the AC. However, the measurements of waveform shape used here can be affected by the SNR of the oscillatory activity used to quantify them. In particular, higher SNR of oscillatory activity in FAF (which is apparent in **Fig. 1**) could result in narrower distributions of cycle features, because low SNR increases the dispersion of waveform shape features (see Schaworonkow and Nikulin (2019)). The SNR for burst detection is controlled by the parameter amplitude fraction threshold, which discards cycles below a certain amplitude percentile calculated from all cycles in an LFP trace (Cole and Voytek, 2019; Schaworonkow and Voytek, 2021). Therefore, to test whether the results shown above can be simply accounted for by different SNR levels in FAF and AC, we evaluated the sensitivity of the inter-areal differences to different values of amplitude fraction threshold in FAF and AC (**Fig. 5**).

The median effect size of inter-areal comparison was used as a summary metric of differences in median feature values (**Fig. 5a, b**) and CV values (**Fig. 5c, d**) across cortical regions. This metric corresponds to the median value of the upper-right quadrant of the comparison matrices in **Figs. 3** and **4**. We systematically varied the amplitude fraction threshold parameter (range: 0.1 – 0.9, step of 0.1) used to detect oscillatory bursts independently in the FAF or the AC, and for each iteration we calculated the median effect size of inter-areal comparisons. As depicted in **Fig. 5a**, period values for delta-band cycles were different between FAF and AC with typically medium or even low effect sizes ($|d| < 0.5$ for low, $0.5 <= |d| < 0.8$ for medium), while asymmetries differed with typically strong effect sizes ($|d| > 0.8$) almost regardless of the amplitude fraction threshold value used. In general, observations across threshold values in delta- and gamma-bands (**Fig. 5b** for gamma) were well in line with the data depicted in **Fig. 3**. Those data were obtained with a parameter value of 0.5 (red squares in **Fig. 5**). Similarly, CVs were consistently lower in FAF than in AC across a wide range of amplitude fraction threshold values in both delta- and gamma- frequency bands (**Fig. 5c**, delta; **Fig. 5d**, gamma), and for all three cycle features considered. These data were consistent with those shown in **Fig. 4**. The results indicate that the differences in waveform shape features and their CV values between frontal and auditory cortices are not trivially accounted for by differences in SNR across regions.

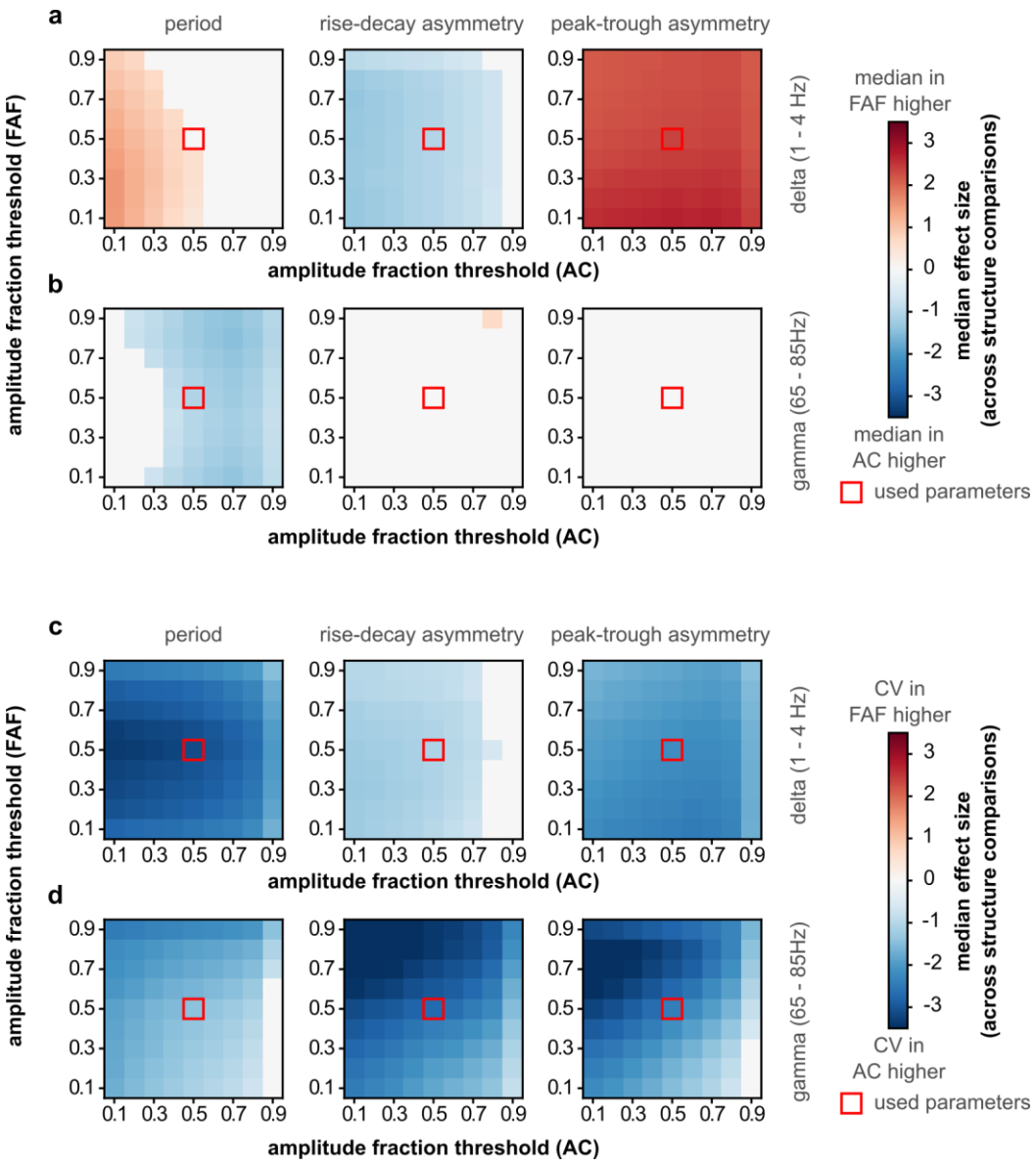

Figure 5. Differences in regularity across structures are robust against variations of burst detection amplitude threshold. The burst detection parameter "amplitude fraction threshold" was varied independently in FAF and AC to determine whether SNR critically contributes to differences in oscillatory regularity between frontal and auditory areas. The difference across regions was measured as the median effect size obtained from comparing all pairs of channels in FAF and AC (e.g. median of the upper right quadrant in the comparison matrices in **Fig. 3a**, labelled "inter-areal comparisons"). In the absence of significant differences (FDR-corrected Wilcoxon signed rank tests, $p_{corr} < 0.05$), effect size values were set to 0 ($p_{corr} >= 0.05$). (**a**) Median effect sizes across all values of amplitude fraction threshold tested in FAF and AC, for delta frequencies, comparing the median of cycle periods (left), cycle rise-decay asymmetries (middle) and cycle peak-trough asymmetries (right). (**b**) Same as in **a**, but data corresponds to cycles from gamma-band oscillatory bursts. (**c**, **d**) Same as in **a**, **b**, but the CV was calculated across cycle periods. Red squares indicate the amplitude fraction threshold values used to detect bursts used in the main results.

A conceptual model captures patterns of waveform shape differences between FAF and AC

We hypothesized that differences across areas, particularly when considering the CV of waveform features, might reflect the activity of two distinct cortical generators exhibiting different degrees of regularity. We illustrate this idea with a conceptual model in which an oscillation occurs as a consequence of the temporally aligned rhythmic discharge of a population of neurons. This conceptualization makes no assumption on the nature of the neuronal oscillators themselves (see Discussion); instead, it only

assumes that extracellular oscillatory activity occurs when a sufficiently large neuronal population fires concertedly (Buzsaki et al., 2012). We reasoned that a highly synchronous population firing would lead to a strong current at a given phase of the LFP resulting in relatively asymmetric waveform shape; by contrast, a relatively asynchronous population activity would yield less asymmetric temporal features. We simulated 30 neurons firing rhythmically for 150 seconds at a gamma rate (60 Hz, for illustrative purposes; this can be generalized to other frequencies as well), with varying degrees of synchronicity among them. The synchronicity was controlled by varying the width of the time window in which neurons would fire in a Poisson-like manner. This was done by changing the duty cycle of pulses in a square pulse train. Lower duty cycles represent narrower spiking windows and therefore higher synchronicity across neurons (**Fig. 6a**). From the neuronal firing in each condition, we generated a synthetic LFP by convoluting each spike train with a synaptic kernel and adding them over all neurons. This synthetic LFP was used to estimate cycle features computed with the *bycycle* algorithm, analogue to the analyses performed on the empirical data.

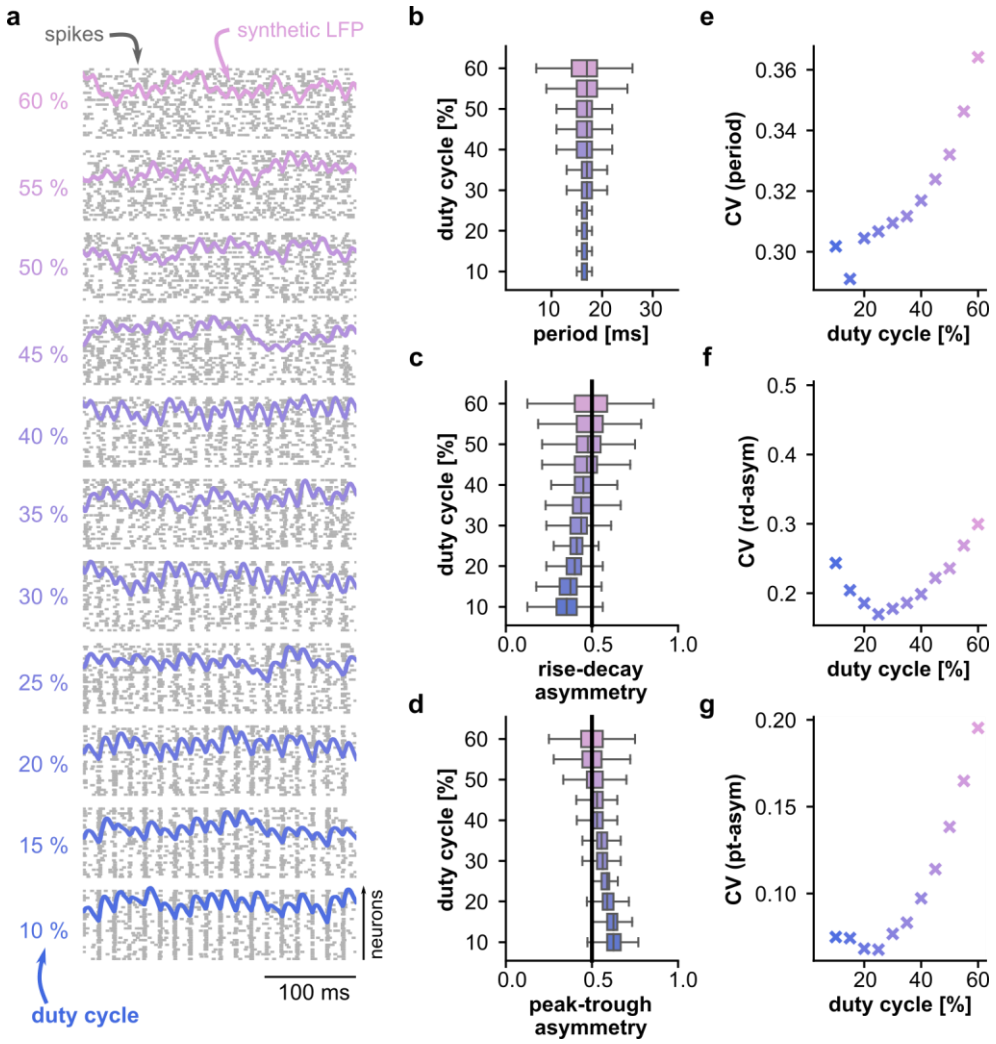

Figure 6. A linear model captures the differences in waveform shape between FAF and AC. (**a**) Representative spiking activity of a population of N=30 simulated neurons (length: 300 ms). The synchronicity across neurons varies with the duty cycle of a pulse train modulating firing rate

(lower duty cycle, more synchronous; see Methods). A synthetic LFP was calculated for each condition. (**b-d**) The period (**b**), rise-decay asymmetry (**c**), and peak-trough asymmetry (**d**) values across all cycles detected by the *bycycle* algorithm for each duty cycle tested. The black line in panels **c** and **d** represents no asymmetry (i.e. a value of 0.5). (**e-g**) CV values of features period (**h**), rise-decay asymmetry (**i**), and peak-trough asymmetry (**j**). In panels **b-g**, values from each duty cycle simulation are colour coded according to panel **a**.

Figure **6b-d** illustrates the distribution of cycle features (**Fig. 6b**, period; **Fig. 6c**, rise-decay asymmetry; **Fig. 6d**, peak-trough asymmetry) across duty cycle conditions. Across duty cycles we did not observe a change in the median period, but we did observe a consistent change in temporal asymmetries indicating that, as the population became less synchronous (higher duty cycles), the waveform of the synthetic LFP cycles gradually became less asymmetric (**Fig. 6c**, **d**; black line at 0.5 indicates a lack of temporal asymmetry). Indeed, the median of the temporal asymmetries settled at 0.5 for duty cycles >= 50% (**Fig 6f, g**). In addition, we observed that higher duty cycles resulted in broader distributions, as illustrated by the fact that the CV across waveform features tended to increase with duty cycle (even beyond 50%, when no differences existed in the median of the features). Thus, as the population became less synchronized feature values became more variable. These two cases (higher asymmetry for more synchronized population spiking and more variability for less synchronized spiking) reflect differences in delta- and gamma-band oscillations in FAF and AC, and offer a simple yet plausible account of the patterns observed across regions.

These results suggest that differences in FAF and AC waveform shape can at least be partially accounted for by different degrees of synchronicity in the underlying neuronal firing. To test this prediction, we turned to the spiking activity in frontal and auditory regions (**Fig. 7a**). We hypothesized that neuronal spiking would be more highly correlated in FAF than in AC and, additionally, more strongly synchronized with oscillations in the LFP (a secondary consequence of the model in **Fig. 6**). For each recording, we averaged correlation coefficients obtained from FAF and AC channels, and tested whether their values were significantly different across regions. These analyses corroborated that spike train correlations were higher in frontal regions (**Fig. 7b**, bottom; Wilcoxon signed-rank test, $p=2x10^{-6}$) with a large effect size (d = 0.84).

Because delta-band oscillations exhibited the largest differences in terms of asymmetry (**Fig. 3**), we studied spike-LFP relationships in this frequency range. Here, only spikes occurring within oscillatory bursts, as detected by the *bycycle* algorithm, were considered (note that these are the same bursts used in **Figs. 3** and **4**). Spike times were expressed as the point of spike occurrence relative to the period of the burst cycle in which they occurred (0, spike occurs at beginning of cycle; 1, spike occurs at end of cycle), and spike phases were obtained by multiplying the relative spike timing by 2π. The distribution of spike phases form the recordings shown in **Fig. 7a** are depicted in **Fig. 7c** (N = 6709 spikes in FAF, N = 221 spikes in AC), suggesting a tighter clustering of spike phases in FAF. The pairwise phase consistency (PPC; Vinck et al. (2010)) was computed for all channels across recordings. The PPC measures how tightly spike phases group together (phase consistency) and constitutes a bias-free equivalent to the square of the phase locking value. Higher PPC values indicate higher spike-LFP

coherence. To test whether spikes in FAF were more strongly synchronized to delta-band LFPs than those in the AC, we averaged PPC values across channels in FAF and AC (as described above) and statistically compared consistency across regions. PPC values were significantly higher in FAF than in AC (**Fig. 7d**, bottom; Wilcoxon signed-rank test, $p=1.67\times10^{-3}$) with a large effect size (d = 0.89).

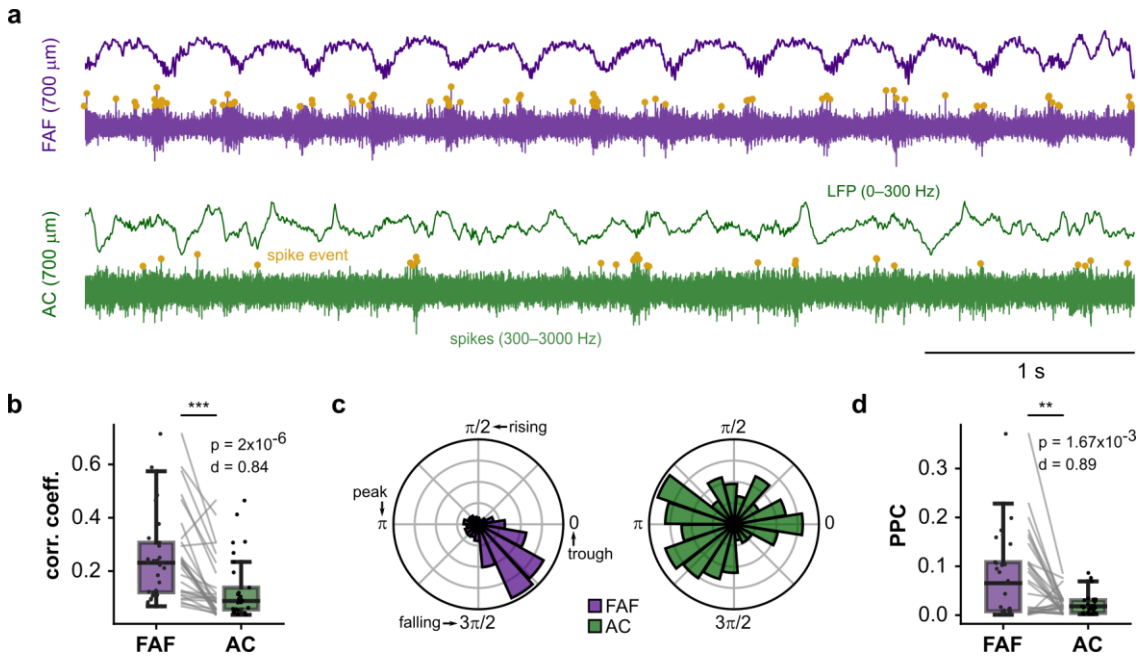

Figure 7. Spiking activity in FAF is more correlated and more strongly synchronized to delta-band oscillatory bursts. (**a**) Representative LFP (top) and spiking (bottom) activity from FAF (purple) and AC (green) electrodes at depths of 700 μm. (b) Spike-spike correlation coefficients for each recording in FAF and AC (N = 29; averaged across channels); spike-spike correlation in FAF was significantly larger than in AC (Wilcoxon signed-rank test, $p=2\times10^{-6}$, d = 0.84, large effect size). (**c**) Distribution of spike phases relative to delta LFPs in FAF (left, N = 6709 spikes) and AC (right, N = 221 spikes). Spikes were only those occurring during bursts of delta-band activity as detected by the *bycycle* algorithm. Troughs, peaks, rising and falling phases, for any given cycle, are indicated in the figure. (**d**) Average PPC values in FAF and AC were compared across all recordings (N = 29). There was significantly larger spike-phase consistency in FAF than in AC (Wilcoxon signed-rank test, $p=1.67\times10^{-3}$, d = 0.89, large effect size).

Altogether, these results show that differences in waveform asymmetries between FAF and AC in delta frequencies are accompanied by differences in spike correlations and spike-LFP synchronization between regions. These observations are in line with predictions derived from the conceptual model illustrated in **Fig. 6**, and support a relationship between waveform shape and spike synchronization. Direct correlations between, for example, peak-trough asymmetry and spike-train correlations were, although significant, relatively weak (FAF, p = 0.025, adjusted R^2 = 0.14; AC, p = 0.009, adjusted R^2 = 0.2), indicating that oscillatory waveform shape cannot be trivially explained by local spike synchronization alone.

Discussion

In this work, oscillations in the bat frontal and auditory cortices were studied with respect to their waveform shape. We show that oscillations present in simultaneously recorded LFPs in the fronto-auditory circuit differ markedly in waveform shape and in the variability of waveform features across individual cycles. This heterogeneity is not trivially accounted for by different levels of SNR in frontal and

auditory regions. A conceptual model suggests a relationship between the temporal organization of neuronal spiking and waveform shape asymmetry, with higher spike temporal correlations leading to more asymmetric waveforms. In line with the predictions of the model, we demonstrate that spike-spike and spike-LFP correlations differ significantly in the FAF-AC network.

The bat frontal and auditory cortices are two brain regions with distinct cytoarchitectonic patterns, which likely accounts for the differences observed in oscillatory waveform shape across areas. *C. perspicillata*'s AC is a primary sensory region with a well-defined, six-layered columnar structure and clear inter-laminar boundaries (see Garcia-Rosales et al. (2019) for histology), following a blueprint that is typical across mammalian species (Douglas and Martin, 2004; Linden and Schreiner, 2003; Mountcastle, 1997). By contrast, *C. perspicillata*'s FAF lacks clear boundaries between layers (see Garcia-Rosales et al. (2022); Weineck et al. (2020)), mirroring instead the stereotypical agranular or slightly agranular architecture of the mammalian frontal cortex (Beul and Hilgetag, 2014; Camarda and Bonavita, 1985; Shepherd, 2009). Differences between the bat frontal and auditory regions likely extend to other cytoarchitectonic properties such as the distribution of cell-type density and overall cellular organization. Beyond anatomy, cortical cytoarchitecture plays a significant role in defining activity patterns and brain function. Indeed, the functional characteristics of a given region are well-related to its cytoarchitecture (Badre and D'Esposito, 2009; Pandya and Yeterian, 1996), which includes the nature of incoming and outgoing axonal connections (Hilgetag et al., 2019; Kritzer et al., 1992; Passingham et al., 2002), cell-type specific characteristics (e.g. density, morphology; Benavides-Piccione et al. (2002); Beul and Hilgetag (2014)), and laminar organization (Hooks et al., 2011). Local cytoarchitecture affects neuronal firing patterns, which are known to vary consistently across functionally and anatomically well-defined regions (Badre and D'Esposito, 2009; Mochizuki et al., 2016; Shinomoto et al., 2009). Anatomical differences between granular and agranular cortical areas also result in distinct intra- and inter-laminar connectivity patterns (Beul and Hilgetag, 2014; Shepherd, 2009), which may also affect the dynamics of the generators of cortical oscillatory activity. Together, local anatomy, spiking patterns, and connectivity influence mesoscopic measurements of activity such as LFPs or other signals recorded non-invasively (Buzsaki et al., 2012; Cole and Voytek, 2017).

Other than local cytoarchitecture, respiration can also affect both single-neuron and oscillatory activities (Tort et al., 2018). For example, respiratory rhythms in mice entrain single neuron spiking and local cortical oscillations particularly –but not only- in frontal regions, (Koszeghy et al., 2018; Tort et al., 2018) with measurable functional consequences (Bagur et al., 2021; Folschweiller and Sauer, 2023). Respiratory rhythms were not measured in this study, and therefore their potential effects cannot be directly ruled out. For example, it is possible that respiration influences the patterns of rhythmicity and asymmetry overserved in frontal areas by directly modulating the LFP, by synchronizing neuronal spiking and then altering the LFPs as a consequence, or a combination of both these scenarios. Future studies should clarify the roles –if any- of respiration in modifying oscillatory waveform shape dynamics.

Delta-band oscillations differed markedly across regions in terms of their temporal asymmetries, something that did not occur consistently for gamma-band activity (**Fig. 3**). However, for both frequency ranges we observed large and consistent inter-areal differences in the variability of shape feature values across individual cycles (**Fig. 4**). A conceptual model (**Fig. 6**) suggests that temporal asymmetries (i.e. waveform shape features) and their variability across cycles (measured with the CV), could depend on the degree of correlated activity of the underlying neuronal population. The model in **Fig. 6** suggests that more synchronous populations yield highly asymmetric waveform shape and lower cycle-by-cycle variability, while less synchronous populations yield gradually a more sinusoidal shape with more variable cycle-by-cycle features. Below a certain degree of synchronicity (e.g. for duty cycles higher than 50% in **Fig. 6**), temporal asymmetries settle to values close to 0.5 (no asymmetry) but the distribution of feature values continues to broaden, which would account for the effects observed in gamma frequencies across FAF and AC. That waveforms become less asymmetric can be explained by temporal averaging of the contribution of each spike to the LFP, akin to the expected effects of spatial averaging in electro- or magneto-encephalographic recordings (Schaworonkow and Nikulin, 2019). Note that the model does not make any assumptions about important features of the underlying generators, such as location in the local circuitry, connectivity patterns, or component cell-types. As discussed above, these factors can influence both waveform shape and spiking dynamics. Instead, the model provides a parsimonious account of the empirical data shown in **Fig. 3**, assuming only that spiking is an important contributor to the LFP (Buzsaki et al., 2012). The model in **Fig. 6**, together with the waveform shape differences across regions, affords one prediction, namely that spike-spike and spike-LFP correlations should be higher in the area with more asymmetric signals (i.e. the FAF). Our results in **Fig. 7** corroborate such prediction, illustrating that the bat frontal cortex exhibits more correlated spiking, which is also more strongly synchronized the ongoing LFP phase in delta frequencies. As a concept, and supported by our data, the model draws a relationship between waveform shape asymmetry and the temporal dynamics of neuronal spiking in the neocortex.

A hypothesis stemming from the above observations is that differences in the CV of cycle features between frontal and auditory cortical areas might be explained by different values of temporal correlations in their underlying generators. In other words, it could be speculated that putative generators in the FAF operate with tighter parameters (reflected in higher temporal correlations) than their AC counterparts. One possible take on the functional implications of such phenomenon would be that frontal circuits rely more on internal timescales, while auditory circuits exhibit an elevated flexibility and perturbability. Previous studies have demonstrated that activity patterns in the rodent prefrontal cortex exhibit less variability than those of sensory regions (Castano-Prat et al., 2017; Ruiz-Mejias et al., 2011), potentially reflecting a cortical hierarchy of excitability and circuit properties. In such hierarchy, peripheral areas exhibit more adaptability to sensory stimuli (and therefore more variability), while frontal areas exhibit higher stimulus independence, yielding activity patterns better related to local network dynamics (Badre and D'Esposito, 2009; Braun and Mattia, 2010; Ruiz-Mejias et al., 2011)). In the bat brain, the FAF appears to be a

modulation and control structure that may also be involved in the integration of diverse inputs during echolocation and navigation, as reflected by its internal dynamics and by the anatomical and functional connectivity patterns with other cortical and subcortical regions (Casseday et al., 1989; Eiermann and Esser, 2000; Garcia-Rosales et al., 2022; Kanwal et al., 2000; Kobler et al., 1987; Weineck et al., 2020). Conversely, the bat AC (as that of other mammals) is primarily tasked with representing sounds that may unfold in time over nested timescales, typically exhibiting varying degrees of periodicity which require higher adaptability and flexibility (Doelling et al., 2019; Garcia-Rosales et al., 2018; Henry and Obleser, 2012; Lakatos et al., 2013; Teng et al., 2017). Indeed, previous modelling work suggests that neuronal response patterns in FAF and AC can be accounted by slower synaptic dynamics in the frontal region (Lopez-Jury et al., 2020), something that could be detrimental for precise stimulus tracking but that could be important for sensory integration. From the above, we hypothesize that a higher level of variability in the auditory cortical circuitry (**Fig. 4**) might aid with efficient sensory representations in AC (see Pittman-Polletta et al. (2021)), while narrower dynamics could be important for high-level computations in FAF (e.g. sensory integration), closely tied to internal timescales and more robust against external perturbations.

In conclusion, we have shown that simultaneously recorded oscillatory activity across frontal and auditory cortices differs markedly in waveform shape. Additionally, a conceptual model, paired with empirical results, suggests a relationship between waveform shape and local spiking activity. This intriguing relationship could serve as a tool for constraining generative models of neural oscillations, and can be used to draw hypotheses after observing waveform shape differences across experimental conditions. Our data indicate that oscillations in frontal and auditory regions with similar frequencies possess nevertheless distinct dynamics reflecting the heterogeneous anatomical and functional properties of the bat fronto-auditory network.

Methods

Animal preparation and surgical procedures

The study was conducted on two awake *Carollia perspicillata* bats (2 males), which were obtained from a colony at the Goethe University, Frankfurt. All experimental procedures were in compliance with European regulation and were approved by the relevant local authorities (Regierungspräsidium Darmstadt, experimental permit #FU-1126). Experimental subjects were kept isolated from the main colony.

The data presented in this work were collected as part of a previous study (Garcia-Rosales et al., 2022), where a detailed description of the surgical procedures can be found. In brief, bats were anesthetized with a mixture of ketamine (10 mg*kg^{-1}, Ketavet, Pfizer) and xylazine (38 mg*kg^{-1}, Rompun, Bayer), and underwent surgery in order to expose the skull in the areas of the frontal and auditory cortices. A metal

rod (ca. 1 cm length, 0.1 cm diameter) was glued onto the bone for head fixation during electrophysiological recordings. A local anaesthetic (ropivacaine hydrochloride, 2 mg/ml, Fresenius Kabi, Germany) was applied subcutaneously around the scalp area prior any handling of the wounds. The precise locations of the FAF and AC were determined by means of well-described landmarks, including the sulcus anterior and prominent blood vessel patterns (Eiermann and Esser, 2000; Esser and Eiermann, 1999; Garcia-Rosales et al., 2020). Access to the frontal and auditory regions of the left hemisphere was gained by cutting small holes (ca. 1 mm^2) with a scalpel blade on the first day of recordings. Electrophysiological recordings in the AC were made mostly in the high frequency fields (Esser and Eiermann, 1999).

After the surgery animals were given sufficient time to recover (no less than 2 days) before the beginning of experimental sessions. A session did not last more than 4 hours per day. Water was offered to the bats every 1 – 1.5 hours. Experiments were halted if an animal showed any signs of discomfort (e.g. as excessive movement). No animal was used on two consecutive days for recordings.

Electrophysiological recordings

Electrophysiological measurements were made acutely from fully awake animals in a sound-proofed and electrically isolated chamber. Inside the chamber, bats were placed on a custom-made holder kept at a constant temperature of 30 °C using a heating blanket (Harvard, Homeothermic blanket control unit). Data were acquired simultaneously from the FAF and AC of the left hemisphere using two 16-channel laminar probes (Model A1x16, NeuroNexus, MI; 50 µm channel spacing, impedance: 0.5–3 MΩ per electrode). For each paired FAF-AC recording, probes were carefully inserted into the tissue using piezo manipulators (one per probe; PM-101, Science products GmbH, Hofheim, Germany), perpendicular to the cortical surface, until the top channel was barely visible above the surface. The typical width of *C. perspicillata*'s cortex, and the total span of the probes (750 µm) allowed us to record from all six cortical layers at once (see Garcia-Rosales et al. (2022); Garcia-Rosales et al. (2019)). Probes in FAF and AC were connected to micro-preamplifiers (MPA 16, Multichannel Systems MCS GmbH, Reutlingen, Germany), while acquisition was done with a single 32-channel system with integrated digitization (sampling frequency, 20 kHz; precision, 16 bits) and amplification steps (Multi Channel Systems MCS GmbH, model ME32 System, Germany)s. Silver wires were used as references electrodes for each recording shank (i.e. in FAF and AC) placed at different areas of the brain (for FAF: non-auditory lateral ipsilateral region; for AC: non-auditory occipital ipsilateral region). The silver wires were carefully positioned between the skull and the dura matter. The reference and the ground of each probe were short-circuited, and the ground was ultimately common in the acquisition system (the ME32). Recordings were monitored online and stored in a computer using the MC_Rack_Software (Multi Channel Systems MCS GmbH, Reutlingen, Germany; version 4.6.2). Due to technical reasons, the signal from one FAF channel (depth: 500 µm) was linearly interpolated from its immediate neighbours.

Pre-processing of spiking and LFP signals

All data analyses were made using custom-written Python scripts. Raw data from the recording system were converted to H5 format using Multichannel System's *McsPyDataTools* package (https://github.com/multichannelsystems/McsPyDataTools, version 0.4.3), and were then parsed and handled with Syncopy (https://github.com/esi-neuroscience/syncopy, version 2022.8). Local-field potentials were obtained by filtering the raw data with a low pass Butterworth filter (4th order) with a cut-off frequency of 300 Hz. For computational convenience, LFP signals were then downsampled to 1 kHz. For the detection of multi-unit activity, the raw data was bandpass filtered between 300 and 3000 Hz with a 4th order Butterworth filter. Spikes were detected based on threshold crossing: we defined a spike as a peak with an amplitude of at least 3.5 standard deviations relative all samples in the signal. Only peaks separated by at least 2 ms were considered.

Spectral analyses

Power spectral densities (PSDs) like the ones shown in **Fig. 1a** were computed using Welch's method (segment length 4096 samples –same in ms) implemented in *scipy* (version 1.9.1). PSDs were calculated independently for each paired FAF-AC penetration (N = 29) and channel, corresponding to ~20 minutes LFP traces per recording. The power of each recording was parametrized using a spectral parametrization model (Donoghue et al., 2020), with which a 1/f fit of the PSD was computed. All fits had an $R^2 > 0.93$ (mean: 0.9965, s.e.m.: 0.001).

We reasoned that significant deviations of the power spectrum from the 1/f fit potentially represented oscillatory activity at a given frequency range. Thus, we normalized each power spectrum by its 1/f component to highlight spectral peaks in FAF and AC. Normalized values would hover around 0 in the case of no spectral peaks, and would be consistently greater than 0 for frequencies in which LFPs presented clear deviations from the underlying 1/f trend. For each channel, we considered a significant deviation from the 1/f if the normalized power at a certain frequency was significantly larger than 0 (FDR-corrected, two-sided one-sample t-tests, $p_{corr} < 0.05$). This analysis was done for each individual animal (**Bat-01**, N = 15; **Bat-02**, N = 14), for frequencies ranging from 1 to 120 Hz. From the results in the two bats, we established the following frequency bands of interest: delta (1-4 Hz) and gamma (65-85 Hz).

Cycle-by-cycle analyses

For detecting oscillatory bursts in the frequencies of interest we used the *bycycle* package ((Cole and Voytek, 2019), version 1.0.0). The *bycycle* algorithm makes it possible to detect individual cycles in frequency range of interest (here, the frequency bands outlined above), and then to determine whether detected cycles belong to so-called "oscillatory" bursts. An oscillatory burst consists of a sequence of cycles (at least 3 in this study) with stable temporal properties that are mainly summarized as follows: amplitude consistency, period consistency, and monotonicity (rise and decay flanks of cycles in a burst

should be mostly monotonic). Furthermore, one parameter controls for signal-to-noise ratio (SNR): the amplitude fraction threshold (see **Fig. 2a**). This parameter rejects cycles whose amplitudes are below a certain percentile relative to the amplitude of all cycles in a given trace. As in (Schaworonkow and Voytek, 2021), we chose the following thresholds for cycle detection: Amplitude fraction threshold, 0.5; Amplitude consistency threshold, 0.5; Period consistency threshold, 0.5; Monotonicity threshold, 0.5.

Each cycle was characterized according to the following features, which determine waveform shape: cycle period (i.e. the duration of each cycle), cycle rise-decay asymmetry (the asymmetry between rise and decay times in the cycle), and cycle peak-trough asymmetry (the asymmetry in duty cycle; see also (Cole and Voytek, 2019; Schaworonkow and Voytek, 2021)). Bursts were characterized according to their duration (the sum of the individual duration of each cycle in the burst) and the number of cycles that composed them. Only cycles that were part of oscillatory bursts were used for further analyses.

The aforementioned cycle features characterize waveform shape, but they do not quantify to what degree burst cycles in a given LFP trace are more similar to one another. This is measured by the dispersion of the distribution of the cycle features, which was quantified here as the coefficient of variation (CV). The CV is expressed as follows:

$$CV = \frac{\sigma_W}{\mu_W} \quad , \qquad [1]$$

where σ_W is the standard deviation of the cycle feature distribution (*W*), and μ_W its mean.

Every recording in frontal and auditory cortices had a specific CV for a given cycle parameter, channel and frequency band. This enabled us to conduct paired statistics when comparing CV values between FAF and AC, since our data consisted of simultaneous individual recordings in both areas (N = 29 recordings, 15 in **Bat-01** and 14 in **Bat-02**; FDR-corrected Wilcoxon signed-rank tests, significant for $p_{corr} < 0.05$). The cycle features themselves were compared across channels in a similar manner (for each penetration, the median and not the CV across all burst cycles was calculated). The latter comparisons answers, for example, whether waveform shape differed across structures.

<u>Sensitivity analyses</u>

To evaluate the dependence of significant differences across cortical structures on the burst detection parameters of the *bycycle* algorithm, bursts were detected as above but detection parameters were varied in pairs as follows: (i) amplitude fraction threshold vs. amplitude consistency threshold; (ii) amplitude fraction threshold vs. period consistency threshold; and (iii) amplitude fraction threshold vs. monotonicity threshold. The same parameter values were used to detect bursts in FAF and AC. However, we also evaluated to what degree our results were sensitive to different burst detection parameters across regions, varying the amplitude fraction threshold independently in each area (**Fig. 5**). Parameters

were varied in the range from 0.1 to 0.9, with a step of 0.1. All waveform features were computed as described above, and the dispersion of waveform feature distributions was measured as the CV. As in the original analyses, all channels were statistically compared against each other. We then determined the median of the effect size of comparisons across areas (i.e. the median effect size of the upper-right quadrant of the comparison matrices in **Figs. 3, 4**; effect sizes of non-significant comparisons were set to 0), and plotted this median against parameter combinations (**Figs. 5**) to establish how changing detection parameters affected the reported inter-areal differences.

Spike-spike correlations

All detected spiking events (see above) were included to calculate spike train correlations across channels. Spike trains were binned using 5 ms bins, and the Pearson's correlation coefficient across pairs of binned spike trains was computed using the *Elephant* toolbox (v. 0.12.0; https://github.com/NeuralEnsemble/elephant). Correlation coefficients from channels located in the FAF were averaged, and the same was done for channels located in the AC. This yielded one correlation value per penetration in FAF and AC, which allowed to capitalize on simultaneous recordings in both regions by means of paired statistical comparisons (Wilcoxon signed-rank test, alpha = 0.05).

Pairwise phase consistency

The pairwise phase consistency (PPC) was computed as described in previous literature (Vinck et al., 2010). Only spikes that occurred within oscillatory bursts in FAF or AC were considered. If more than 10000 spikes were detected in a given trace, for computational reasons 10000 spikes were randomly selected to calculate PPC given that analyses were computationally expensive for larger spike counts. In order to minimize the risk of asymmetric signals yielding unclear measurements of phase, spike phases were not obtained by means of a Hilbert transform or a Fourier analysis. Instead, the timing of a spike was expressed as the time in which the event occurred relative the onset and offset of a cycle as detected in the time series by the *bycycle* algorithm. Thus, each spike timing was between 0 and 1 (0 being the beginning of a burst cycle, 1 being the end), and was converted to a phase by multiplication with 2π. These phases were then used for PPC calculation, which can be expressed as follows (Vinck et al., 2010):

$$PPC = \frac{2}{N(N-1)} \sum_{j=1}^{N-1} \sum_{k=(j+1)}^{N} f(\phi_j, \phi_k), \qquad [2]$$

where N is the number of spikes, and ϕ_j, ϕ_k represent the phases of spikes *j* and *k*, respectively. The function $f(\phi_j, \phi_k)$ calculates the dot product between two unit vectors. It can be expressed as follows:

$$f(\phi_j, \phi_k) = \cos(\phi_j)\cos(\phi_k) + \sin(\phi_j)\sin(\phi_k) \qquad [3]$$

PPC values were averaged in FAF and AC, and paired statistical comparisons were made to evaluate whether significant differences in spike phase consistency existed between regions (Wilcoxon signed-rank test, alpha = 0.05).

Statistics and reproducibility

All statistical analyses were performed using scipy (version 1.9.1), or custom written Python scripts. For determining significant deviations from a 1/f fitted trend in the LFP spectra one-sample t-tests were performed. Statistical comparisons of median and CV values across regions (and within regions) were performed using paired statistics (Wilcoxon signed-rank tests, alpha = 0.05), as recordings in FAF and AC were performed simultaneously (N = 29). Comparisons of spike-spike and spike-LFP correlation (PPC values) were also made using paired statistics. Tests were corrected for multiple comparisons using the false discovery rate when appropriate (Benjaminin and Hochberg procedure (Benjamini and Hochberg, 1995)); it is noted in the main text whenever this correction was applied.

Acknowledgments

This work was supported by the DFG (Grant No. HE 7478/1-1, to J.C.H.), the Joachim-Herz Foundation (fellowship granted to F.G.R.), and a Marie Skłodowska-Curie Actions Postdoctoral Fellowship (grant No. 101062497, to N.S.).

Contributions

F.G.R, N.S., J.C.H. and conceived and designed the research. F.G.R collected and analysed the data, produced original figures, and wrote the first draft of the manuscript. F.G.R., N.S, and J.C.H. discussed analyses and results, interpreted data, and reviewed figures and text.

Conflict of interests

The authors declare no conflicting financial or non-financial interests.

References

Badre, D., and D'Esposito, M. (2009). Is the rostro-caudal axis of the frontal lobe hierarchical? Nature Reviews Neuroscience *10*, 659-669.

Bagur, S., Lefort, J.M., Lacroix, M.M., de Lavilleon, G., Herry, C., Chouvaeff, M., Billand, C., Geoffroy, H., and Benchenane, K. (2021). Breathing-driven prefrontal oscillations regulate maintenance of conditioned-fear evoked freezing independently of initiation. Nat Commun *12*, 2605.

Baranauskas, G., Maggiolini, E., Vato, A., Angotzi, G., Bonfanti, A., Zambra, G., Spinelli, A., and Fadiga, L. (2012). Origins of 1/f2 scaling in the power spectrum of intracortical local field potential. J Neurophysiol *107*, 984-994.

Benavides-Piccione, R., Ballesteros-Yanez, I., DeFelipe, J., and Yuste, R. (2002). Cortical area and species differences in dendritic spine morphology. J Neurocytol *31*, 337-346.

Benjamini, Y., and Hochberg, Y.J.J.o.t.R.s.s.s.B. (1995). Controlling the false discovery rate: a practical and powerful approach to multiple testing. *57*, 289-300.

Beul, S.F., and Hilgetag, C.C. (2014). Towards a "canonical" agranular cortical microcircuit. Front Neuroanat *8*, 165.

Braun, J., and Mattia, M. (2010). Attractors and noise: twin drivers of decisions and multistability. Neuroimage *52*, 740-751.

Buzsaki, G., Anastassiou, C.A., and Koch, C. (2012). The origin of extracellular fields and currents--EEG, ECoG, LFP and spikes. Nat Rev Neurosci *13*, 407-420.

Camarda, R.M., and Bonavita, V. (1985). The frontal agranular cortex and the organization of purposeful movements. Ital J Neurol Sci *6*, 287-315.

Casseday, J.H., Kobler, J.B., Isbey, S.F., and Covey, E. (1989). Central acoustic tract in an echolocating bat: an extralemniscal auditory pathway to the thalamus. J Comp Neurol *287*, 247-259.

Castano-Prat, P., Perez-Zabalza, M., Perez-Mendez, L., Escorihuela, R.M., and Sanchez-Vives, M.V. (2017). Slow and Fast Neocortical Oscillations in the Senescence-Accelerated Mouse Model SAMP8. Front Aging Neurosci *9*, 141.

Cohen, J. (2013). Statistical power analysis for the behavioral sciences (Routledge).

Cole, S., and Voytek, B. (2019). Cycle-by-cycle analysis of neural oscillations. J Neurophysiol *122*, 849-861.

Cole, S.R., van der Meij, R., Peterson, E.J., de Hemptinne, C., Starr, P.A., and Voytek, B. (2017). Nonsinusoidal Beta Oscillations Reflect Cortical Pathophysiology in Parkinson's Disease. J Neurosci *37*, 4830-4840.

Cole, S.R., and Voytek, B. (2017). Brain Oscillations and the Importance of Waveform Shape. Trends Cogn Sci *21*, 137-149.

Doelling, K.B., Assaneo, M.F., Bevilacqua, D., Pesaran, B., and Poeppel, D. (2019). An oscillator model better predicts cortical entrainment to music. Proc Natl Acad Sci U S A *116*, 10113-10121.

Donoghue, T., Haller, M., Peterson, E.J., Varma, P., Sebastian, P., Gao, R., Noto, T., Lara, A.H., Wallis, J.D., Knight, R.T*., et al.* (2020). Parameterizing neural power spectra into periodic and aperiodic components. Nat Neurosci *23*, 1655-1665.

Douglas, R.J., and Martin, K.A. (2004). Neuronal circuits of the neocortex. Annu Rev Neurosci *27*, 419-451.

Eiermann, A., and Esser, K.H. (2000). Auditory responses from the frontal cortex in the short-tailed fruit bat Carollia perspicillata. Neuroreport *11*, 421-425.

Esser, K.H., and Eiermann, A. (1999). Tonotopic organization and parcellation of auditory cortex in the FM-bat Carollia perspicillata. Eur J Neurosci *11*, 3669-3682.

Folschweiller, S., and Sauer, J.F. (2023). Behavioral State-Dependent Modulation of Prefrontal Cortex Activity by Respiration. J Neurosci *43*, 4795-4807.

Garcia-Rosales, F., Beetz, M.J., Cabral-Calderin, Y., Kossl, M., and Hechavarria, J.C. (2018). Neuronal coding of multiscale temporal features in communication sequences within the bat auditory cortex. Commun Biol *1*, 200.

Garcia-Rosales, F., Lopez-Jury, L., Gonzalez-Palomares, E., Cabral-Calderin, Y., and Hechavarria, J.C. (2020). Fronto-Temporal Coupling Dynamics During Spontaneous Activity and Auditory Processing in the Bat Carollia perspicillata. Front Syst Neurosci *14*, 14.

Garcia-Rosales, F., Lopez-Jury, L., Gonzalez-Palomares, E., Wetekam, J., Cabral-Calderin, Y., Kiai, A., Kossl, M., and Hechavarria, J.C. (2022). Echolocation-related reversal of information flow in a cortical vocalization network. Nat Commun *13*, 3642.

Garcia-Rosales, F., Rohrig, D., Weineck, K., Rohm, M., Lin, Y.H., Cabral-Calderin, Y., Kossl, M., and Hechavarria, J.C. (2019). Laminar specificity of oscillatory coherence in the auditory cortex. Brain Struct Funct *224*, 2907-2924.

Gourevitch, B., Martin, C., Postal, O., and Eggermont, J.J. (2020). Oscillations in the auditory system and their possible role. Neurosci Biobehav Rev *113*, 507-528.

Gross, J., Schnitzler, A., Timmermann, L., and Ploner, M. (2007). Gamma oscillations in human primary somatosensory cortex reflect pain perception. PLoS Biol *5*, e133.

Hechavarria, J.C., Beetz, M.J., Macias, S., and Kossl, M. (2016). Vocal sequences suppress spiking in the bat auditory cortex while evoking concomitant steady-state local field potentials. Sci Rep *6*, 39226.

Helfrich, R.F., and Knight, R.T. (2019). Cognitive neurophysiology of the prefrontal cortex. Handb Clin Neurol *163*, 35-59.

Henry, M.J., and Obleser, J. (2012). Frequency modulation entrains slow neural oscillations and optimizes human listening behavior. Proc Natl Acad Sci U S A *109*, 20095-20100.

Hilgetag, C.C., Beul, S.F., van Albada, S.J., and Goulas, A. (2019). An architectonic type principle integrates macroscopic cortico-cortical connections with intrinsic cortical circuits of the primate brain. Netw Neurosci *3*, 905-923.

Hooks, B.M., Hires, S.A., Zhang, Y.X., Huber, D., Petreanu, L., Svoboda, K., and Shepherd, G.M. (2011). Laminar analysis of excitatory local circuits in vibrissal motor and sensory cortical areas. PLoS Biol *9*, e1000572.

Insel, N., Patron, L.A., Hoang, L.T., Nematollahi, S., Schimanski, L.A., Lipa, P., and Barnes, C.A. (2012). Reduced gamma frequency in the medial frontal cortex of aged rats during behavior and rest: implications for age-related behavioral slowing. J Neurosci *32*, 16331-16344.

Jackson, N., Cole, S.R., Voytek, B., and Swann, N.C. (2019). Characteristics of Waveform Shape in Parkinson's Disease Detected with Scalp Electroencephalography. eNeuro *6*.

Kanwal, J.S., Gordon, M., Peng, J.P., and Heinz-Esser, K. (2000). Auditory responses from the frontal cortex in the mustached bat, Pteronotus parnellii. Neuroreport *11*, 367-372.

Kienitz, R., Cox, M.A., Dougherty, K., Saunders, R.C., Schmiedt, J.T., Leopold, D.A., Maier, A., and Schmid, M.C. (2021). Theta, but Not Gamma Oscillations in Area V4 Depend on Input from Primary Visual Cortex. Curr Biol *31*, 635-642 e633.

Kobler, J.B., Isbey, S.F., and Casseday, J.H. (1987). Auditory pathways to the frontal cortex of the mustache bat, Pteronotus parnellii. Science *236*, 824-826.

Koszeghy, A., Lasztoczi, B., Forro, T., and Klausberger, T. (2018). Spike-Timing of Orbitofrontal Neurons Is Synchronized With Breathing. Front Cell Neurosci *12*, 105.

Kritzer, M.F., Cowey, A., and Somogyi, P. (1992). Patterns of inter- and intralaminar GABAergic connections distinguish striate (V1) and extrastriate (V2, V4) visual cortices and their functionally specialized subdivisions in the rhesus monkey. J Neurosci *12*, 4545-4564.

Lakatos, P., Chen, C.M., O'Connell, M.N., Mills, A., and Schroeder, C.E. (2007). Neuronal oscillations and multisensory interaction in primary auditory cortex. Neuron *53*, 279-292.

Lakatos, P., Musacchia, G., O'Connel, M.N., Falchier, A.Y., Javitt, D.C., and Schroeder, C.E. (2013). The spectrotemporal filter mechanism of auditory selective attention. Neuron *77*, 750-761.

Lakatos, P., Shah, A.S., Knuth, K.H., Ulbert, I., Karmos, G., and Schroeder, C.E. (2005). An oscillatory hierarchy controlling neuronal excitability and stimulus processing in the auditory cortex. J Neurophysiol *94*, 1904-1911.

Linden, J.F., and Schreiner, C.E. (2003). Columnar transformations in auditory cortex? A comparison to visual and somatosensory cortices. Cereb Cortex *13*, 83-89.

Lopez-Jury, L., Mannel, A., Garcia-Rosales, F., and Hechavarria, J.C. (2020). Modified synaptic dynamics predict neural activity patterns in an auditory field within the frontal cortex. Eur J Neurosci *51*, 1011-1025.

Luo, H., and Poeppel, D. (2007). Phase patterns of neuronal responses reliably discriminate speech in human auditory cortex. Neuron *54*, 1001-1010.

Medvedev, A.V., and Kanwal, J.S. (2004). Local field potentials and spiking activity in the primary auditory cortex in response to social calls. J Neurophysiol *92*, 52-65.

Mochizuki, Y., Onaga, T., Shimazaki, H., Shimokawa, T., Tsubo, Y., Kimura, R., Saiki, A., Sakai, Y., Isomura, Y., Fujisawa, S.*, et al.* (2016). Similarity in Neuronal Firing Regimes across Mammalian Species. J Neurosci *36*, 5736-5747.

Mountcastle, V.B. (1997). The columnar organization of the neocortex. Brain *120 (Pt 4)*, 701-722.

Neymotin, S.A., Tal, I., Barczak, A., O'Connell, M.N., McGinnis, T., Markowitz, N., Espinal, E., Griffith, E., Anwar, H., Dura-Bernal, S.*, et al.* (2022). Detecting Spontaneous Neural Oscillation Events in Primate Auditory Cortex. eNeuro *9*.

Pandya, D.N., and Yeterian, E.H. (1996). Comparison of prefrontal architecture and connections. Philos Trans R Soc Lond B Biol Sci *351*, 1423-1432.

Passingham, R.E., Stephan, K.E., and Kotter, R. (2002). The anatomical basis of functional localization in the cortex. Nat Rev Neurosci *3*, 606-616.

Pittman-Polletta, B.R., Wang, Y., Stanley, D.A., Schroeder, C.E., Whittington, M.A., and Kopell, N.J. (2021). Differential contributions of synaptic and intrinsic inhibitory currents to speech segmentation via flexible phase-locking in neural oscillators. PLoS Comput Biol *17*, e1008783.

Rajan, A., Siegel, S.N., Liu, Y., Bengson, J., Mangun, G.R., and Ding, M. (2019). Theta Oscillations Index Frontal Decision-Making and Mediate Reciprocal Frontal-Parietal Interactions in Willed Attention. Cereb Cortex *29*, 2832-2843.

Ruiz-Mejias, M., Ciria-Suarez, L., Mattia, M., and Sanchez-Vives, M.V. (2011). Slow and fast rhythms generated in the cerebral cortex of the anesthetized mouse. J Neurophysiol *106*, 2910-2921.

Schaworonkow, N., and Nikulin, V.V. (2019). Spatial neuronal synchronization and the waveform of oscillations: Implications for EEG and MEG. PLoS Comput Biol *15*, e1007055.

Schaworonkow, N., and Voytek, B. (2021). Longitudinal changes in aperiodic and periodic activity in electrophysiological recordings in the first seven months of life. Dev Cogn Neurosci *47*, 100895.

Shepherd, G.M. (2009). Intracortical cartography in an agranular area. Front Neurosci *3*, 337-343.

Shinomoto, S., Kim, H., Shimokawa, T., Matsuno, N., Funahashi, S., Shima, K., Fujita, I., Tamura, H., Doi, T., Kawano, K.*, et al.* (2009). Relating neuronal firing patterns to functional differentiation of cerebral cortex. PLoS Comput Biol *5*, e1000433.

Tan, L.L., Oswald, M.J., Heinl, C., Retana Romero, O.A., Kaushalya, S.K., Monyer, H., and Kuner, R. (2019). Gamma oscillations in somatosensory cortex recruit prefrontal and descending serotonergic pathways in aversion and nociception. Nat Commun *10*, 983.

Tavares, L.C.S., and Tort, A.B.L. (2022). Hippocampal-prefrontal interactions during spatial decision-making. Hippocampus *32*, 38-54.

759 Teng, X., Tian, X., Rowland, J., and Poeppel, D. (2017). Concurrent temporal channels for auditory
760 processing: Oscillatory neural entrainment reveals segregation of function at different scales. PLoS Biol
761 *15*, e2000812.
762 Tort, A.B.L., Brankack, J., and Draguhn, A. (2018). Respiration-Entrained Brain Rhythms Are Global but
763 Often Overlooked. Trends Neurosci *41*, 186-197.
764 Uran, C., Peter, A., Lazar, A., Barnes, W., Klon-Lipok, J., Shapcott, K.A., Roese, R., Fries, P., Singer, W., and
765 Vinck, M. (2022). Predictive coding of natural images by V1 firing rates and rhythmic synchronization.
766 Neuron *110*, 2886-2887.
767 Veniero, D., Gross, J., Morand, S., Duecker, F., Sack, A.T., and Thut, G. (2021). Top-down control of visual
768 cortex by the frontal eye fields through oscillatory realignment. Nat Commun *12*, 1757.
769 Vinck, M., van Wingerden, M., Womelsdorf, T., Fries, P., and Pennartz, C.M. (2010). The pairwise phase
770 consistency: a bias-free measure of rhythmic neuronal synchronization. Neuroimage *51*, 112-122.
771 Weineck, K., Garcia-Rosales, F., and Hechavarria, J.C. (2020). Neural oscillations in the fronto-striatal
772 network predict vocal output in bats. PLoS Biol *18*, e3000658.
773 Zhang, S., Xu, M., Chang, W.C., Ma, C., Hoang Do, J.P., Jeong, D., Lei, T., Fan, J.L., and Dan, Y. (2016).
774 Organization of long-range inputs and outputs of frontal cortex for top-down control. Nat Neurosci *19*,
775 1733-1742.

776